Transition properties of low-lying states in ^{28}Si probed via inelastic proton and α scattering

Yoshiko Kanada-En'yo

Department of Physics, Kyoto University, Kyoto 606-8502, Japan

Kazuyuki Ogata

Research Center for Nuclear Physics (RCNP), Osaka University, Ibaraki 567-0047, Japan;
Department of Physics, Osaka City University, Osaka 558-8585, Japan;
and Nambu Yoichiro Institute of Theoretical and Experimental Physics (NITEP), Osaka City University, Osaka 558-8585, Japan

0^+, 1^-, 2^+, and 3^- excitations of ^{28}Si are investigated via proton and α inelastic scattering off ^{28}Si. The structure calculation of ^{28}Si is performed with the energy variation after total angular momentum and parity projections in the framework of antisymmetrized molecular dynamics (AMD). As a result of the AMD calculation, the oblate ground and prolate bands, 0^+ and 3^- excitations, and the 1^- and 3^- states of the $K^\pi = 0^-$ band are obtained. Using the matter and transition densities of ^{28}Si obtained by AMD, microscopic coupled-channels calculations of proton and α scattering off ^{28}Si are performed. The proton-^{28}Si potentials in the reaction calculation are microscopically derived by folding the Melbourne g-matrix NN interaction with the AMD densities of ^{28}Si. The α-^{28}Si potentials are obtained by folding the nucleon-^{28}Si potentials with an α density. The calculation reasonably reproduces the observed elastic and inelastic cross sections of proton and α scattering. Transition properties are discussed by combining the reaction analysis of proton and α scattering and structure features such as transition strengths and form factors. The isoscalar monopole and dipole transitions are focused.

I. INTRODUCTION

One of the interesting phenomena concerning nuclear deformations in sd-shell nuclei is shape coexistence of oblate and prolate deformations of ^{28}Si. The ground band of the 0_1^+, 2_1^+, and 4_1^+ states was assigned to the oblate band from experimental data of the quadrupole moment of the 2_1^+ state and in-band $E2$ transitions. The 0_2^+ state is considered to be a monopole vibration mode on the oblate ground state, whereas the 3_1^- state is discussed as an octupole vibration of the ground state. In addition, the excited $K^\pi = 0^+$ band starting from the 0_3^+ at 6.691 MeV is considered to be a prolate deformation band. On the theoretical side, structure studies of ^{28}Si with mean-field [1] and cluster models [2] have suggested coexistence of the oblate and prolate shapes, while modern mean-field calculations failed to describe the prolate 0_3^+ band [3–5]. In these years, calculations with antisymmetrized molecular dynamics (AMD) [6–8] described the shape coexistence of ^{28}Si and discussed excitations on the oblate and prolate deformations. However, assignments of those excited states to experimental energy levels are remaining issues to be solved.

To clarify deformations and transition properties of these excited states, experiments of inelastic electron scattering (e, e') and proton scattering (p, p') off ^{28}Si have been performed [9–14]. The work of Ref. [14] discussed transition densities from the ground state with reaction analysis of (p, p') data at the incident energy $E_p = 180$ MeV combined

with (e, e') data. Detailed studies were performed mainly for strongly populated states, but not done yet for weak transitions. For example, the (p, p') cross sections of the 2_1^+ and 3_1^- states were described with a reaction model calculation using the transition densities reduced from the charge form factors measured by (e, e') cross sections. For a consistency check, the reduced transition densities were found to give consistent values of $B(E2)$ and $B(E3)$ with those determined by γ-decay lifetimes.

For 0^+ and 1^- states, there are no γ-decay data of the transition strengths. In principle, the transition strengths can be determined by form factors at low momentum transfer q. However, electron-scattering data observed for the 0_2^+ and 1^- states are not enough to determine precise values of the $E0$ and isoscalar dipole (IS1) transition strengths. In the experimental study of (p, p') at $E_p = 180$ MeV [14], a reaction calculation was performed by using the transition densities reduced from the (e, e') data and succeeded in reproducing the cross sections of the 0_2^+ state, but not the 1_1^- (8.89 MeV) state. In the study of (p, p') at $E_p = 65$ MeV [13], they tried to describe 1_1^- (8.89 MeV) and 3_2^- (10.18 MeV) cross sections by assuming an octupole $K^\pi = 0^-$ vibrational band, but the calculation failed to reproduce the 1_1^- (8.89 MeV) data. For the 0_3^+ (6.691 MeV) of the prolate band, there is almost no data of electron or proton scattering because of weak population in the inelastic scattering.

In these two decades, inelastic α scattering (α, α') has been extensively investigated to obtain information about excited states. Especially, the (α, α') reaction has been utilized as a sensitive probe for isoscalar monopole (IS0) and IS1 transitions of excited states as well as giant resonances in various nuclei [15–32]. It is also a useful tool to search for new cluster states because cluster excitations often have strong inelastic transitions [20,33–38]. Along this line, (α, α') experiments at $E_\alpha = 130$ and 386 MeV have been performed for various $Z = N$ nuclei in the sd-shell region, and provided (α, α') cross-section data of the 0_2^+, 0_3^+, and 1^- states of ^{28}Si [32]. Now, it is an important issue to investigate transition properties of excited states with analysis of the (α, α') data combining them with (e, e') and (p, p') data as well as $B(E\lambda)$ values determined by γ decays.

In our previous studies [39,40], we have achieved microscopic coupled-channels (MCC) calculations of α scattering off ^{12}C and ^{16}O and succeeded to reproduce the (α, α') cross sections of various excited states by using matter and transition densities of the target nuclei calculated with AMD [41–43]. We have performed similar MCC calculations of proton scattering for the 2_1^+ states of various $Z \neq N$ nuclei in a light-mass region [44] and have shown that this approach is applicable for proton and α scattering off stable and unstable nuclei.

In this study, we apply the MCC approach to ^{28}Si for calculation of proton and α scattering. In our MCC calculations, the Melbourne g-matrix NN interaction are used to construct proton-nucleus and α-nucleus potentials in a microscopic folding model (MFM). An important feature of this effective NN interaction is that there is no adjustable parameter because it was derived based on bare nucleon-nucleon interactions. The original MFM with the Melbourne g-matrix interaction was developed and applied to proton-nucleus elastic scattering successfully in Ref. [45], and its simplified version has been applied systematically to proton-nucleus [46–48] and α-nucleus [49] elastic scattering. Very recently, this framework was applied to MCC calculations of proton and α inelastic processes using the microscopic matter and transition densities obtained by structure model calculations [39,40,44,48,50].

One of the advantages of the present approach is that one can discuss inelastic processes of different hadron probes, proton and α, in a unified treatment of a microscopic description. Another advantage is that there is no adjustable parameter in the reaction part as mentioned above. Once matter and transition densities are given as structure inputs, one can obtain the (p, p') and (α, α') cross sections at given energies without ambiguity. Owing to this straightforward procedure from structure inputs to output cross sections, one can judge validity of a given structure input via proton and α cross sections even if electric data are not accurate enough to check the input.

In the present paper, we investigate properties of the 0^+, 1^-, 2^+, and 3^- excitations of ^{28}Si via inelastic proton and α scattering with the MCC calculation. A main focus is low-energy IS0 and IS1 excitations from the ground state. As for a microscopic description of structure of ^{28}Si, we use an AMD model. Since the main concern in this paper is inelastic-scattering processes, we focus only on the oblate ground band, the lowest prolate bands, and 1^- and 3^- excitations on the oblate state. In this paper, we start a version of AMD adopted in Ref. [6], that is, variation before angular-momentum projection with fixed nucleon spins. This version was used to describe the oblate and prolate shape coexistence in $N = 14$ isotopes including ^{28}Si. We improve the previous calculation to variation after the angular momentum and parity projections (VAP) for calculation of the ground and excited states of ^{28}Si. With the obtained wave functions, we investigate structure properties such as transition strengths and densities as well as form factors. For the use of target densities in the MCC calculation, theoretical transition densities obtained by the AMD calculation are renormalized to fit experimental data of electric transition strengths and/or charge form factors so as to reduce possible ambiguity from the structure model as much as possible.

The paper is organized as follows: The next section describes frameworks of structure and reaction calculations: the AMD framework for structure of the target nucleus ^{28}Si and the MCC approach for proton-^{28}Si and α-^{28}Si scattering. The AMD result for structure properties is shown in Sec. III, and proton- and α-scattering cross sections obtained by the MCC calculation are discussed in Sec. IV. Combining electric properties and hadron inelastic scattering, transition properties of excited states are discussed in Sec. V. Finally, a summary is given in Sec. VI.

II. METHOD

In this section, the methods of structure and reaction calculations are explained. For the structure part, a VAP version of AMD is applied to ^{28}Si. The reaction calculations of proton and α scattering off ^{28}Si are performed with the MCC approach by using the AMD densities of ^{28}Si, as done in Refs. [39,40,44]. For details, the reader is referred to the previous works and references therein.

A. Antisymmetrized molecular dynamics calculation for structure of ^{28}Si

An AMD wave function of an A-nucleon system is given by a Slater determinant of single-nucleon Gaussian wave functions as

$$\Phi_{\mathrm{AMD}}(\boldsymbol{X}) = \frac{1}{\sqrt{A!}} \mathcal{A}\{\varphi_1, \varphi_2, \ldots, \varphi_A\}, \quad (1)$$

$$\varphi_i = \phi_{\boldsymbol{X}_i} \chi_i \tau_i, \quad (2)$$

$$\phi_{\boldsymbol{X}_i}(\boldsymbol{r}_j) = \left(\frac{2\nu}{\pi}\right)^{3/4} \exp[-\nu(\boldsymbol{r}_j - \boldsymbol{X}_i)^2]. \quad (3)$$

Here $\mathcal{A}$ is the antisymmetrizer, and φ_i is the ith single-particle wave function written by a product of spatial $\phi_{\boldsymbol{X}_i}$, nucleon-spin χ_i, and isospin τ_i wave functions. In the present calculation of ^{28}Si, we choose proton up $(p \uparrow)$, proton down $(p \downarrow)$, neutron up $(n \uparrow)$, neutron down $(n \downarrow)$ for the nucleon-spin and isospin wave functions. $\Phi_{\mathrm{AMD}}(\boldsymbol{X})$ is specified by the set of parameters $\boldsymbol{X} = \{\boldsymbol{X}_1, \boldsymbol{X}_2, \ldots, \boldsymbol{X}_A\}$. Here parameters $\boldsymbol{X}_i$ describe centroid positions of single-nucleon Gaussian wave

packets and are treated as variational parameters independently for all nucleons. This wave function is the same as that used in the previous AMD study of ^{28}Si in Ref. [6]. Using this model wave function, we perform energy variation after total-angular-momentum and parity projections (VAP). Namely, the set of parameters $\{X_i\}$ $(i = 1, \ldots, A)$ for each J^π state are determined by the energy variation for the J^π-projected AMD wave function $P_{MK}^{J\pi}\Phi_{\mathrm{AMD}}(X)$ ($P_{MK}^{J\pi}$ is the angular-momentum and parity projection operator) as

$$\delta \frac{\langle P_{MK}^{J\pi}\Phi_{\mathrm{AMD}}(X)|H|P_{MK}^{J\pi}\Phi_{\mathrm{AMD}}(X)\rangle}{\langle P_{MK}^{J\pi}\Phi_{\mathrm{AMD}}(X)|P_{MK}^{J\pi}\Phi_{\mathrm{AMD}}(X)\rangle} = 0. \qquad (4)$$

Here H is the Hamiltonian operator consisting of the one-body kinetic term t_i, two-body $v_{ij}^{\mathrm{eff}\text{-}2}$ and three-body $v_{ijk}^{\mathrm{eff}\text{-}3}$ terms of effective nuclear interactions, and the Coulomb force $v_{ij}^{\mathrm{Coulomb}}$,

$$H = \sum_i t_i - T_G + \sum_{i<j} v_{ij}^{\mathrm{eff}-2} + \sum_{i<j<k} v_{ijk}^{\mathrm{eff}-3} + \sum_{i<j\in Z} v_{ij}^{\mathrm{Coulomb}}, \qquad (5)$$

where T_G is the center-of-mass (c.m.) kinetic-energy term and subtracted from the total Hamiltonian. Note that the c.m. motion can be exactly removed from the wave function in the AMD framework.

All the parameters for the Gaussian width and effective nuclear interactions are the same as those of Ref. [6] as follows: The width parameter $\nu = 0.15$ fm^{-2} is used. For effective nuclear interactions used in the structure calculation, the MV1 (case 1) central force [51] supplemented by a spin-orbit term of the G3RS force [52,53] is used. The Bartlett, Heisenberg, and Majorana parameters of the MV1 force are $b = h = 0$ and $m = 0.62$, and the spin-orbit strengths are $u_I = -u_{II} = 2800$ MeV. The Coulomb force is also included.

B. Microscopic couple-channels calculation of proton and α scattering off ^{28}Si

Elastic and inelastic cross sections of proton and α scattering off ^{28}Si are calculated with the MCC approach as done in Refs. [39,40,44]. The diagonal and coupling potentials for the nucleon-nucleus system are microscopically calculated by folding the Melbourne g-matrix NN interaction [45] with densities of the target nucleus. The matter and transition densities of ^{28}Si obtained by AMD are used as structure inputs for the target nucleus,

The Melbourne g matrix is an effective interaction containing the density and energy dependencies, which are derived by solving a Bethe-Goldstone equation in a uniform nuclear matter with a bare NN interaction of the Bonn B potential [54]. This interaction was constructed in Ref. [45] and examined by systematic investigations of proton elastic and inelastic scattering off various nuclei at energies from 40 to 300 MeV in Refs. [46–48]. In the present MCC calculation of proton scattering, the spin-orbit term of the potential is not taken into account to avoid complexity.

The α-nucleus potentials are obtained in an extended nucleon-nucleus folding (NAF) model [49] by folding the nucleon-nucleus potentials with an α density. For the α

density, we adopt the one-range Gaussian distribution given in Ref. [55]. In the NAF model, energy and density dependencies of the g-matrix NN interaction are taken into account only in the folding process of the target density. The validity of the NAF model for α elastic scattering is discussed in Ref. [49], and it was successfully applied to α inelastic processes in Refs. [39,40].

III. RESULTS OF STRUCTURE CALCULATION OF ^{28}Si

The 0_1^+ state with an oblate shape is obtained by energy variation with the $J^\pi = 0^+$ projection. 1^- and 3^- excitations on the oblate ground state are obtained by energy variation with the 1^- and 3^- projections, respectively. We label the 1^- state as 1_{IS1}^- because of its significant IS1 transition strength. The 3^- state corresponds well to the experimental 3_1^- (6.879 MeV) state, as discussed later, and is labeled as 3_1^-. A vibration 0^+ excitation of the ground state, which we label as 0_{vib}^+, is obtained by the 0^+-projected energy variation for orthogonal component to the 0_1^+ state. A prolate 0^+ state is obtained as a local minimum with the 0^+-projected energy variation. This state is assigned to the bandhead state of the prolate band and labeled as 0_{pro}^+. As a result of VAP, we obtain five AMD wave functions for 0_1^+, 1_{IS1}^-, 3_1^-, 0_{vib}^+, and 0_{pro}^+, which are labeled as $\Phi_{\mathrm{AMD}}(X^{(n)})$ with the index $n = 1, \ldots, 5$ for the five states. These AMD wave functions $\Phi_{\mathrm{AMD}}(X^{(n)})$ $(n = 1, \ldots, 5)$ are regarded as the intrinsic wave functions for the corresponding states.

Density distributions of the intrinsic wave functions $\Phi_{\mathrm{AMD}}(X^{(n)})$ are shown in Fig. 1. The ground state has an approximately oblate shape with the deformation parameter $\beta = 0.28$ [Fig. 1(a)]. The 0_{vib}^+ state is expressed by linear combination of the oblate and spherical wave functions shown in Figs. 1(a) and 1(b), respectively, and regarded as a vibration 0^+ excitation built on the oblate ground state. In addition to the oblate state, the prolate deformation with $\beta = 0.41$ is obtained for the 0_{pro}^+ state as shown in Fig. 1(c). It constructs a prolate rotational band. In the intrinsic density of the 1_{IS1}^- state in Fig. 1(d), one can see formation of an α cluster at the nuclear surface. This state is interpreted as an $K^\pi = 0^-$ excitation mode generated by α-cluster motion on the oblate state. The 3_1^- state shows a triangle deformation on the oblate state.

To calculate energy spectra and wave functions of $J^\pi = 0^+$, 1^-, 2^+, 3^-, and 4^+ states, we superpose configurations by using the five AMD wave functions $\Phi_{\mathrm{AMD}}(X^{(n)})$ $(n = 1, \ldots, 5)$ obtained for 0_1^+, 1_{IS1}^-, 3_1^-, 0_{vib}^+, and 0_{pro}^+. Namely, to express the J_k^π states, the J^π eigen wave functions $P_{MK}^{J\pi}\Phi_{\mathrm{AMD}}(X^{(n)})$ projected from the basis wave functions $\Phi_{\mathrm{AMD}}(X^{(n)})$ $(n = 1, \ldots, 5)$ are superposed as

$$\Psi(J_k^\pi) = \sum_{n,K} c_K^{(n)}(J_k^\pi) P_{MK}^{J\pi}\Phi_{\mathrm{AMD}}^{(n)}, \qquad (6)$$

where coefficients $c_K^{(n)}(J_k^\pi)$ of the linear combination are determined by diagonalization of the norm and Hamiltonian matrices $\langle P_{MK}^{J\pi}\Phi_{\mathrm{AMD}}^{(n)}|P_{MK'}^{J\pi}\Phi_{\mathrm{AMD}}^{(n')}\rangle$ and $\langle P_{MK}^{J\pi}\Phi_{\mathrm{AMD}}^{(n)}|H|P_{MK'}^{J\pi}\Phi_{\mathrm{AMD}}^{(n')}\rangle$, respectively. As a result of the superposition of the
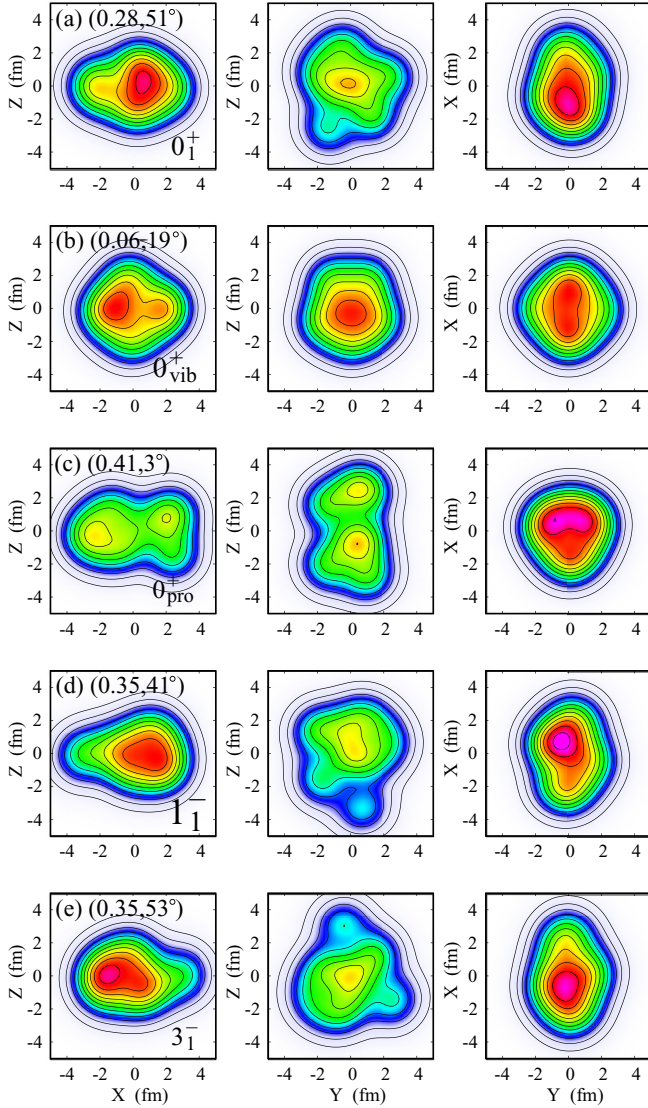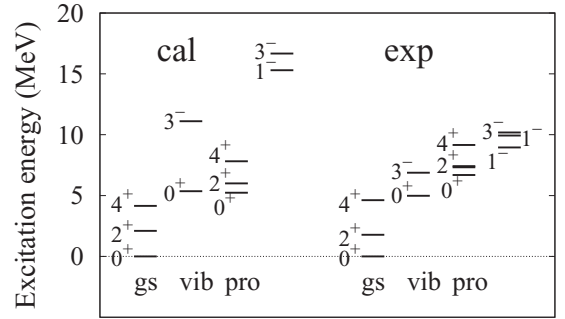
FIG. 1. Density distribution of intrinsic wave functions before the parity and angular-momentum projections for the 0_1^+, 0_{vib}^+, 0_{pro}^+, 1_{IS1}^-, and 3_1^- states of ^{28}Si obtained by AMD. The density projected onto X-Z, Y-Z, and Y-X planes are shown in the left, middle, and right panels, respectively. Here, intrinsic axes are chosen as $\langle ZZ \rangle \geqslant \langle YY \rangle \geqslant \langle XX \rangle$ and $\langle XY \rangle = \langle YZ \rangle = \langle ZX \rangle = 0$. The deformation parameters (β, γ) calculated from the values of $\langle ZZ \rangle$, $\langle YY \rangle$, and $\langle XX \rangle$ are shown in each panel.

J_k^π-projected wave functions, the final wave functions for the 0_1^+, 1_{IS1}^-, 3_1^-, 0_{vib}^+, and 0_{pro}^+ states and their rotational band members are obtained. The binding energy of ^{28}Si is calculated to be 213.3 MeV, which somewhat underestimates the experimental value 236.53 MeV.

Note that the angular-momentum and parity projections as well as the c.m. motion are properly treated in the microscopic way in the present AMD framework. The configuration mixing and K mixing are taken into account by the K and n summation in Eq. (6). Rotations, in-band structure changes, and also vibrations are described with the projections and the configuration mixing. The expectation values of an $\mathcal{O}$ for the
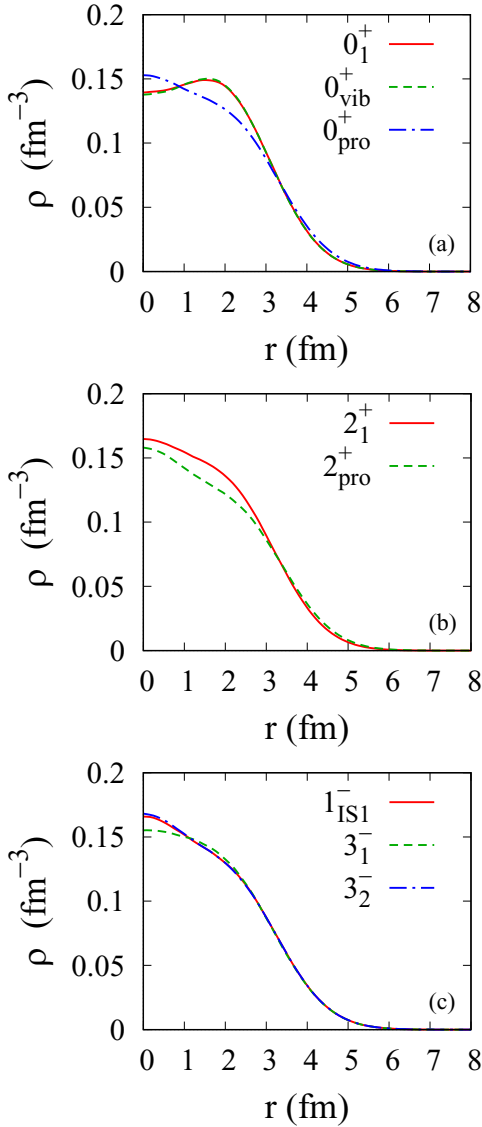

FIG. 2. Energy spectra of ^{28}Si. (left) Calculated energy spectra of the ground and prolate bands, 0_{vib}^+ and 3_1^- excitations of the ground band, and the $K^\pi = 0^-$ band of the 1_{IS1}^- and 3_2^- states. (right) Experimental spectra corresponding to the theoretical states.

J_k^π state are calculated for the final wave functions as

$$\langle \Psi(J_k^\pi) | \mathcal{O} | \Psi(J_k^\pi) \rangle, \tag{7}$$

and the matrix elements for the $J_k^\pi \to J_{k'}'^{\pi'}$ transition are given as

$$\langle \Psi(J_k^\pi) | \mathcal{O} | \Psi(J_{k'}'^{\pi'}) \rangle. \tag{8}$$

Based on analyses of intrinsic structure and transition strengths, we classify the obtained energy levels into the ground band of the 0_1^+, 2_1^+, and 4_1^+ states, the vibration states of the 0_{vib}^+ and 3_1^- states, the prolate band of the 0_{pro}^+, 2_{pro}^+, and 4_{pro}^+ states, and the $K^\pi = 0^-$ band of the 1_{IS1}^- and 3_2^- states. The calculated energy spectra are shown in Fig. 2 and compared with the experimental data. Values of the calculated excitation energies and root-mean-square radii as well as experimental energies are listed in Table I. The radial distribution of matter density is shown in Fig. 3. Excited states

TABLE I. Excitation energies and root mean square radii of ^{28}Si. Calculated values obtained by AMD and experimental values are listed. The theoretical 0_{vib}^+ and 0_{pro}^+ are assigned to the experimental 0_2^+ and 0_3^+ states. Assignment of the theoretical 2_{pro}^+, 4_{pro}^+, 1_1^-, and 3_2^- states are tentative. The experimental energies are from Ref. [56]. The experimental data of the point-proton rms radius of the ground state is $R = 3.010(24)$ fm from the experimental charge radius [57].

Expt.		AMD		
J^π	E_x (MeV)	J^π	E_x (MeV)	R (fm)
0_1^+	0	0_1^+	0.0	3.17
0_2^+	4.98	0_{vib}^+	5.4	3.17
0_3^+	6.691	0_{pro}^+	5.2	3.31
2_1^+	1.779	2_1^+	2.1	3.22
2_2^+	7.32	2_{pro}^+	6.0	3.34
2_3^+	7.42			
4_1^+	4.618	4_1^+	4.1	3.23
(4_3^+)	9.16	4_{pro}^+	7.8	3.34
1_1^-	8.95	1_{IS1}^-	15.3	3.29
1_2^-	9.93			
3_1^-	6.879	3_1^-	11.1	3.28
(3_2^-)	10.18	3_2^-	16.7	3.29

FIG. 3. Matter densities of the 0^+, 2^+, 1^-, and 3^- states of ^{28}Si calculated with AMD.

in the prolate and $K^\pi = 0^-$ bands have larger matter radii than the states in the ground band. However, the state dependence of matter densities is not so large and may give only minor contribution to inelastic scattering of these states.

The result of the $E0$, $E2$, $E3$, and IS1 transition strengths are listed in Table II. As for the ground band, the calculation gives strong in-band transitions of $2_1^+ \to 0_1^+$ and $4_1^+ \to 2_1^+$ consistently with the experimental $B(E2)$ values. For the prolate band, the experimental levels of the 0_3^+ (6.691), 2_2^+ (7.32 MeV), and 4_3^+ (9.16 MeV) are assigned to the rotational band members because the $E2$ transition from 4_3^+ (9.16 MeV) is the strongest to the 2_2^+ (7.32 MeV) state. However, the observed $E2$ transition from 4_3^+ is fragmented also to the 2_3^+ (7.42 MeV) state, which suggests significant state mixing of the prolate 2^+ state. In the present calculation, we obtain the prolate band members, 0_{pro}^+, 2_{pro}^+, and 4_{pro}^+, with almost no fragmentation of the 2_{pro}^+ state. The calculated $B(E2; 4_{pro}^+ \to$

2_{pro}^+) is consistent with a sum of the experimental strengths for the two states, 2_2^+ (7.32 MeV) and 2_3^+ (7.42 MeV). As for the 0_{vib}^+ state, the calculation gives a slightly higher energy than the 0_{pro}^+ state. The energy ordering of the 0_{vib}^+ and 0_{pro}^+ states is not consistent with the experimental data of the 0_2^+ at 4.98 MeV and the 0_3^+ at 6.69 MeV, which are assigned to the vibration and prolate states, respectively.

The calculated $E0$ transition strength of $0_1^+ \to 0_{vib}^+$ is remarkably large and agrees with the experimental $B(E0)$ value for the 0_2^+ (4.98 MeV) reduced from the (e, e') experiment. On the other hand, for the 0_{pro}^+ state, we obtain a relatively weak $E0$ transition because of the shape difference from the ground state. It should be commented that the value of $B(E0; 0_1^+ \to 0_{pro}^+)$ is sensitive to the relative energy between the 0_{vib}^+ and 0_{pro}^+ states. In the present case, the 0_{vib}^+ and 0_{pro}^+ states almost degenerate with each other. This accidental degeneracy somewhat enhances the $B(E0; 0_1^+ \to 0_{pro}^+)$ via the state mixing. It means that the predicted value of $B(E0; 0_1^+ \to 0_{pro}^+)$ may contain model ambiguity and should be checked by experimental observables of inelastic scattering, as discussed later.

As for the negative-parity states 1_{IS1}^-, 3_1^-, and 3_2^-, the calculation tends to overestimate the experimental excitation energies, but it gives reasonable result for inelastic transitions compared with γ-decay and (e, e') data of the 1_1^- (8.95 MeV), 3_1^- (6.88 MeV), and 3_2^- (10.18 MeV) states. The calculation obtains the strong $E3$ transition to the 3_1^- state with the triangle shape on the oblate deformation, which is consistent with the observed $B(E3)$ value of 3_1^- (6.88 MeV).

The 1_{IS1}^- state is characterized by the significant IS1 transition, which is induced by the $K^\pi = 0^-$ excitation mode between mass-asymmetric clusters; that is, the α-cluster motion against the ^{24}Mg core. It is consistent with the theoretical work of Ref. [8] which discussed the remarkable IS1 transition of the 1^- state in the $K^\pi = 0^-$ band. The calculated IS1 transition strength of $1_{vib}^- \to 0_1^+$ is in reasonable agreement with the experimental $B(IS1)$ value of the 1_1^- (8.95 MeV) reduced from the (e, e') experiment. Therefore, we tentatively assign the 1_{IS1}^- state to the 1_1^- (8.95 MeV) state. However, it should be noted that the 1_2^- (9.93) state in the experimental spectra can be another candidate for the 1_{IS1}^- state because the IS1 transitions observed by (e, e') [9,14] for the 1_1^- (8.95 MeV) and 1_1^- (9.93 MeV) states are almost the same order as shown later. The α-cluster excitation constructs the $K^\pi = 0^-$ band consisting of the 1_{IS1}^- and 3_2^- states. The calculated $E3$ transition of $3_2^- \to 0_1^+$ is consistent with the (e, e') data for the 3_2^- (10.18 MeV) state.

For the use of the MCC calculation, transition densities $\rho^{tr}(r)$ are calculated with the obtained AMD wave functions as done in Ref. [39]. To reduce model ambiguity from the structure calculation, the obtained transition densities are renormalized by adjusting the calculated $E\lambda$ transition strength $B_{theor}(E\lambda)$ to the observed strength $B_{expt}(E\lambda)$ as $\rho^{tr}(r) \to f^{tr}\rho^{tr}(r)$ with the factor $f^{tr} = \sqrt{B_{expt}(E\lambda)/B_{theor}(E\lambda)}$. The renormalization factors are determined for the $2_1^+ \to 0_1^+$, $2_1^+ \to 0_1^+$, $0_2^+ \to 2_1^+$, $0_3^+ \to 2_1^+$, and $3_1^- \to 0_1^+$ transitions with the $B_{expt}(E\lambda)$ values of γ-decay lifetimes, and $0_2^+ \to 0_1^+$ and $1_1^- \to 0_1^+$ with the $B_{expt}(E\lambda)$

TABLE II. The $E\lambda$ ad IS1 transition strengths of ^{28}Si calculated with AMD and the experimental values measured by γ-decay lifetimes and electron scattering. For the IS1 transition strengths of the $1^- \to 0^+$ transitions, the values of $B(\mathrm{IS1})/4$ are shown. Values of the renormalization factor f_{tr} are determined by the ratio of the experimental value $B_{\mathrm{expt}}(E\lambda)$ to the calculated value $B_{\mathrm{calc}}(E\lambda)$ as $f_{\mathrm{tr}} = \sqrt{B_{\mathrm{expt}}(E\lambda)/B_{\mathrm{calc}}(E\lambda)}$. For the $3_2^- \to 0_1^+$ transition, $f_{\mathrm{tr}} = 1.40$ is chosen to fit the inelastic form factors of the (e,e') data [9]. The experimental data $B(E\lambda)$ are values reduced from γ-decay lifetimes [56] and the (e,e') data [9,14].

	Expt.		AMD		
	$B(E\lambda)$ [56]	(e,e') [9,14]		$B(E\lambda)$	f_{tr}
$B(E0)$ (e^2 fm^4)					
$0_2^+ \to 0_1^+$		4.71	$0_{\mathrm{vib}}^+ \to 0_1^+$	4.0	1.08
$0_3^+ \to 0_1^+$			$0_{\mathrm{pro}}^+ \to 0_1^+$	0.7	
$B(\mathrm{IS1})/4$ (e^2 fm^6)					
$1_1^- \to 0_1^+$		18.7	$1_1^- \to 0_1^+$	34	0.75
$B(E2)$ (e^2 fm^4)					
$2_1^+ \to 0_1^+$	67(3)	55.7	$2_1^+ \to 0_1^+$	46	1.21
$2_2^+ \to 0_1^+$	1.87(0.76)	1.26	$2_2^+ \to 0_1^+$	0.03	
$2_3^+ \to 0_1^+$	0.82(0.09)	0.90			
$0_2^+ \to 2_1^+$	48(3)		$0_{\mathrm{vib}}^+ \to 2_1^+$	79	0.78
$0_3^+ \to 2_1^+$	1.3(0.1)		$0_{\mathrm{pro}}^+ \to 2_1^+$	15.6	0.29
$4_1^+ \to 2_1^+$	82.8(9.1)		$4_1^+ \to 2_1^+$	87	
$4_3^+ \to 2_1^+$	0.4(0.1)		$4_{\mathrm{pro}}^+ \to 2_1^+$	0.01	
$4_3^+ \to 2_2^+$	152(20)		$4_{\mathrm{pro}}^+ \to 2_{\mathrm{pro}}^+$	236	
$4_3^+ \to 2_3^+$	56.1(9.1)				
$3_1^- \to 1_1^-$			$3_1^- \to 1_1^-$	4.7	
$3_2^- \to 1_1^-$			$3_2^- \to 1_1^-$	75	
$B(E3)$ (e^2 fm^6)					
$3_1^- \to 0_1^+$	615(70)	553(107)	$3_1^- \to 0_1^+$	366	1.30
$3_2^- \to 0_1^+$		78(20)	$3_2^- \to 0_1^+$	76	1.40
$B(E0)$ (e^2 fm^4)					
$4_1^+ \to 0_1^+$		2734	$4_1^+ \to 0_1^+$	2500	

values reduced by the (e,e') experiment. The adopted values of f^{tr} are listed in Table II. For the $3_2^- \to 0_1^+$ transition, $f^{\mathrm{tr}} = 1.40$ is chosen so as to fit the charge form factors. For other transitions, the original transition densities are used as is without renormalization.

The renormalized form factors for positive- and negative-parity states are compared with experimental data in Figs. 4 and 5, respectively. The inelastic form factors of the 0_{vib}^+, 2_1^+, 3_1^-, and 3_2^- states are reproduced reasonably by the calculation after the renormalization. For the 1^- state, the observed form factors of 1_1^- (8.95 MeV) and 1_2^- (9.93 MeV) measured by (e,e') experiment are similar to each other. The result of the 1_{IS1}^- state is in reasonable agreement with the form factors of the two 1^- states and suggests a possible assignment to either of these two states. For the 2_{pro}^+ state, the calculation predicts considerable suppression of the inelastic transitions because of structure difference between the oblate and prolate bands. However, the observed form factors of the 2_2^+ (7.32 MeV) state is larger by two orders of magnitude than the calculation. Not only the magnitude but also the q dependence of the observed form factors are different from the calculation. This suggests that the prolate 2^+ state may contain significant mixing of other 2^+ components beyond the present framework. In other words, the inelastic transition of $0_1^+ \to 2_2^+$ probes the mixing component rather than the prolate 2^+ component. It contrasts with the $E2$ transition from the

4_3^+ state, whose dominant contribution is by the prolate 2^+ component.

The renormalized transition densities are shown in Fig. 6. The transition densities from the ground state to the 0_{vib}^+ and 0_{pro}^+ states [Fig. 6(a)] show a similar r behavior having two nodes at almost the same positions though the amplitude for the 0_{pro}^+ is much smaller. In comparison of the transition densities for the 3_1^- and 3_2^- states, one can see a quite different r behavior between the two 3^- states [Fig. 6(d)]: The transition density to the 3_1^- state has a node at 2.5 fm and remarkable amplitudes in the outer region, while that to the 3_2^- has amplitudes in the inner region without a node. This difference can be observed in the form factors shown in Fig. 5. The calculated form factors show different dip positions between the 3_1^- and 3_2^- states and seem consistent with the (e,e') data.

IV. RESULTS OF PROTON AND α SCATTERING

The MCC calculations of proton scattering at incident energies $E_p = 65$, 100, and 180 MeV and α scattering at incident energies $E_\alpha = 120$, 130, 240, and 400 MeV are performed by using the matter and renormalized transition densities obtained by AMD. In the MCC calculations, we take into account $\lambda = 0$, 1, 2, 3 transitions between the 0_1^+, 0_{vib}^+, 0_{pro}^+, 1_{IS1}^-, 2_1^+, 2_{pro}^+, 3_1^-, and 3_2^- states and use the experimental
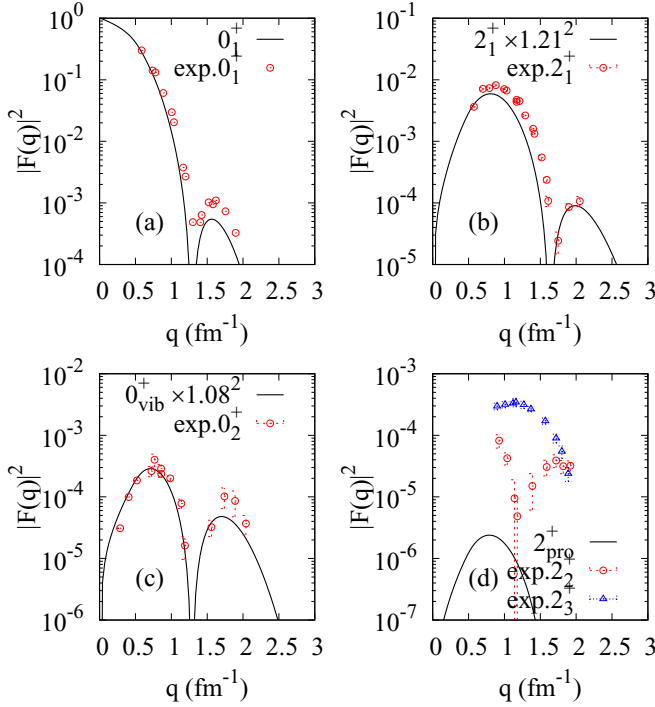
FIG. 4. Elastic and inelastic form factors of positive-parity states of ^{28}Si. The inelastic form factors obtained by AMD are renormalized by f_{tr}^2 with the factor f_{tr} listed in Table II. The experimental data are those measured by electron scattering in Refs. [9,10,14].

FIG. 5. Inelastic form factors of negative-parity states of ^{28}Si. The inelastic form factors obtained by AMD are renormalized by f_{tr}^2 with the factor (f_{tr}) listed in Table II. The experimental data measured by electron scattering are from Refs. [9,10,14]. In panel (a) for the 3_1^- state, triangles indicate the experimental data of the sum of the 3_1^- (6.879 MeV) and 4_2^+ (6.888 MeV) contributions, and circles indicate the 3_1^- (6.879 MeV) data evaluated by subtracting the 4_2^+ (6.888 MeV) contribution from the sum [9].

excitation energies following the assignments to the 0_1^+, 0_2^+ (4.98 MeV), 0_2^+ (4.98 MeV), 2_1^+ (1.779 MeV), 2_2^+ (7.32 MeV), 1_1^- (8.95 MeV), 3_1^- (6.879 MeV), and 3_2^- (10.18 MeV) states, respectively. To see the CC effect, the one-step calculation of the distorted-wave Born approximation (DWBA) is also performed. In the following discussions of the calculated cross sections, we use labels of $0_{1,2,3}^+$, 1_1^-, $2_{1,2}^+$, and $3_{1,2}^-$ corresponding to the above assignments unless otherwise noted.

A. Elastic scattering

In Fig. 7, the elastic proton- and α-scattering cross sections are shown compared with the experimental data. The calculation reasonably reproduces amplitudes of the (p, p) cross sections at $E_p = 65$, 100, and 180 MeV and qualitatively describes diffraction patterns, although it is not precise enough to reproduce dip structure at large angles mainly because the spin-orbit potentials are ignored in the present calculation. At higher energies, even the cross sections around the peaks are undershot for the same reason. For α scattering, the calculation successfully reproduces amplitude and diffraction patterns of the elastic cross sections at $E_p = 240$ and 400 MeV. For lower energies, agreement with the data is reasonable but the observed data are not sufficiently precise for detailed discussions and are even inconsistent between different experiments.
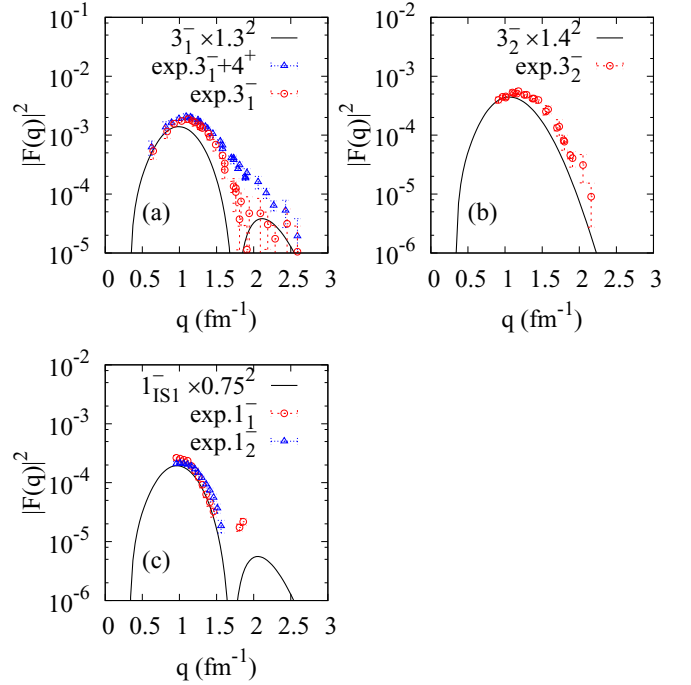
B. Inelastic scattering of proton

Figure 8 shows the (p, p') cross sections of the $0_{2,3}^+$, $2_{1,2}^+$, 1_1^-, and $3_{1,2}^-$ states. Results of the CC (solid lines) and DWBA (dashed lines) calculations are shown together with the experimental data. One can see that the CC effect in proton scattering is generally minor in this energy range. For the 0_2^+, 2_1^+, 3_1^-, and 3_2^- states, the CC calculation reasonably reproduces amplitudes and diffraction patterns of the (p, p') cross sections at forward peaks. It also describes the observed 1_1^- cross sections qualitatively, but the agreement with the experimental data is not satisfactory. For the 2_2^+ state, the calculation fails to reproduce the experimental data: the calculated cross sections are smaller than the data by two orders of magnitude, consistently with the underestimation of the form factors. This result suggests again possible mixing of other component with the prolate component in the 2_2^+ state. As for the 0_3^+ state, there is only a few data of (p, p') cross sections at $E_p = 180$–185 MeV. In the (p, p') experiment at $E_p = 180$ MeV, weak production of the 0_3^+ state has been observed. From the peak hight in the observed spectrum shown in Fig. 1 of Ref. [14], one can roughly estimate the 0_3^+ cross section at $\theta_{c.m.} = 20°$ as $\frac{1}{4}$ of the 0_2^+ cross section. In the experiment at $E_p = 185$ MeV [11], the upper limit of the 0_3^+ cross section at $\theta_{c.m.} = 4°$ was reported. These two data are plotted for order estimation of the 0_3^+ cross sections in Fig. 8. The data seem to be consistent with the calculated 0_3^+ cross
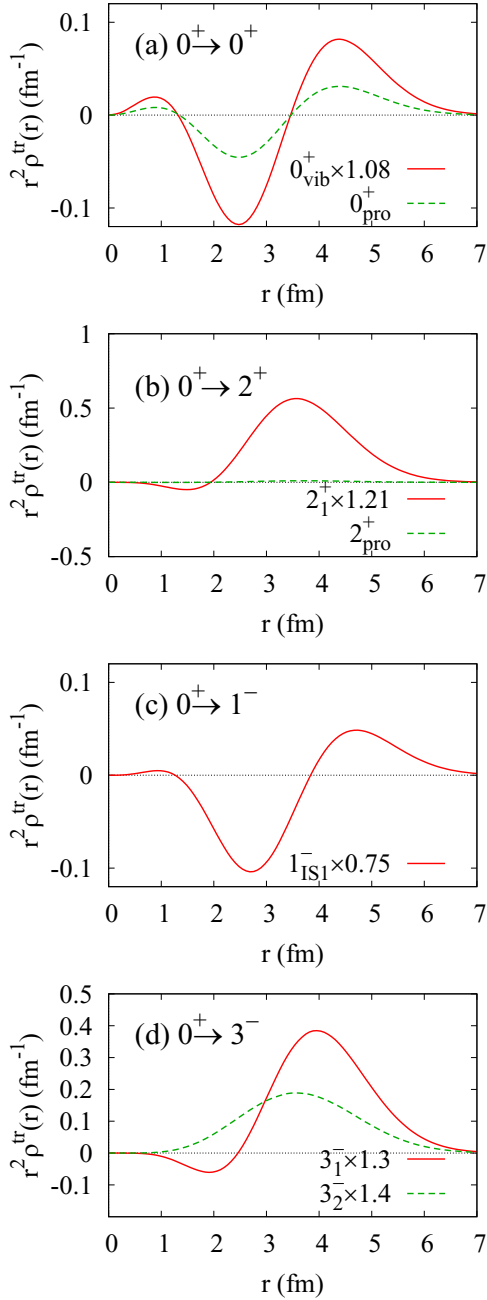
FIG. 6. Transition densities of rank $\lambda = J$ transitions from the ground state to J^π states. The theoretical values calculated with AMD are renormalized by f_{tr} listed in Table II.

sections at $E_p = 180$ MeV, but the quality of the data is not enough to clarify the transition properties of the 0_3^+ state.

C. Inelastic scattering of α

The calculated cross sections for α inelastic scattering at $E_\alpha = 120$, 130, 240, and 400 MeV are shown in Fig. 9 compared with experimental data for $E_\alpha = 120$ [59], 130 [32], 240 [19], and 386 MeV [32]. One can see that the CC effect is significant in the 0_2^+ state and non-negligible in the 3_1^- state, while it is relatively minor in the 0_3^+, 2_1^+, 1_1^-,
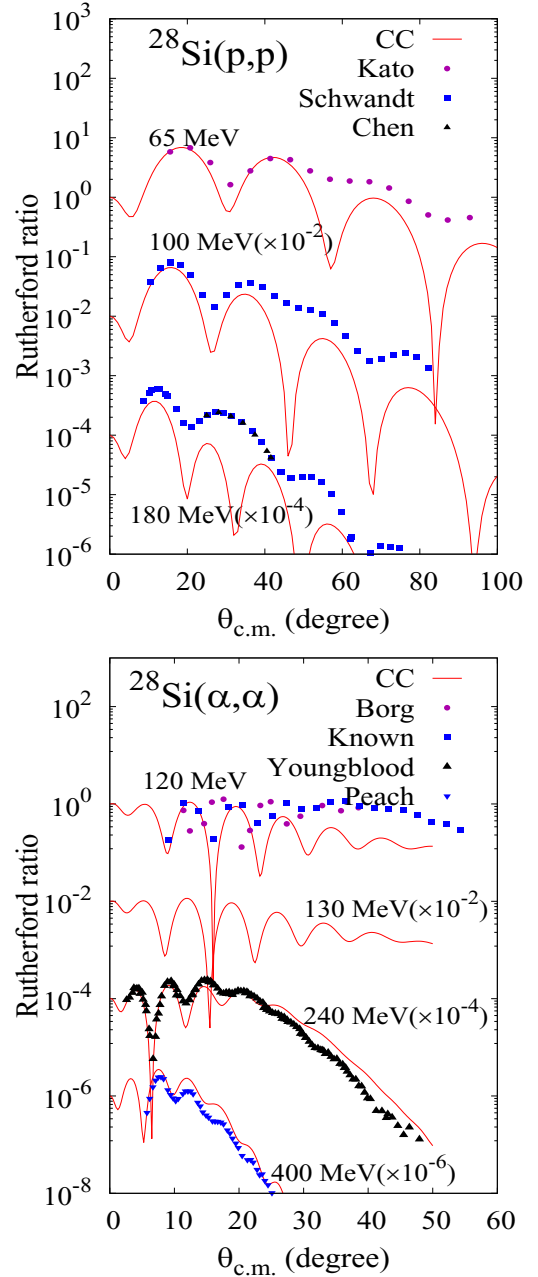
FIG. 7. Cross sections of elastic proton and α scattering off ^{28}Si calculated with the CC calculation for proton incident energies $E_p =$ 65, 100, 180 MeV and α incident energies $E_\alpha = 120$, 130, 240, and 386 MeV. The experimental data are (p, p) cross sections at $E_p =$ 65 MeV [13], 100 MeV [58], and 180 MeV [14], and (α, α) cross sections at $E_\alpha = 120$ MeV [59,60], 240 MeV [19], and 386 MeV [29].

and 3_2^- cross sections. The CC effect becomes weaker as the incident energy increases, as expected. The CC calculation successfully reproduces the 0_2^+, 2_1^+, and 3_1^- cross sections with good description of amplitudes and diffraction patterns in a wide energy range. It also describes well the experimental cross sections of the 0_3^+ state at $E_p = 130$ MeV and those of the 3_2^- state at $E_\alpha = 120$ MeV. These results support the validity of the present MCC approach and the accuracy of the
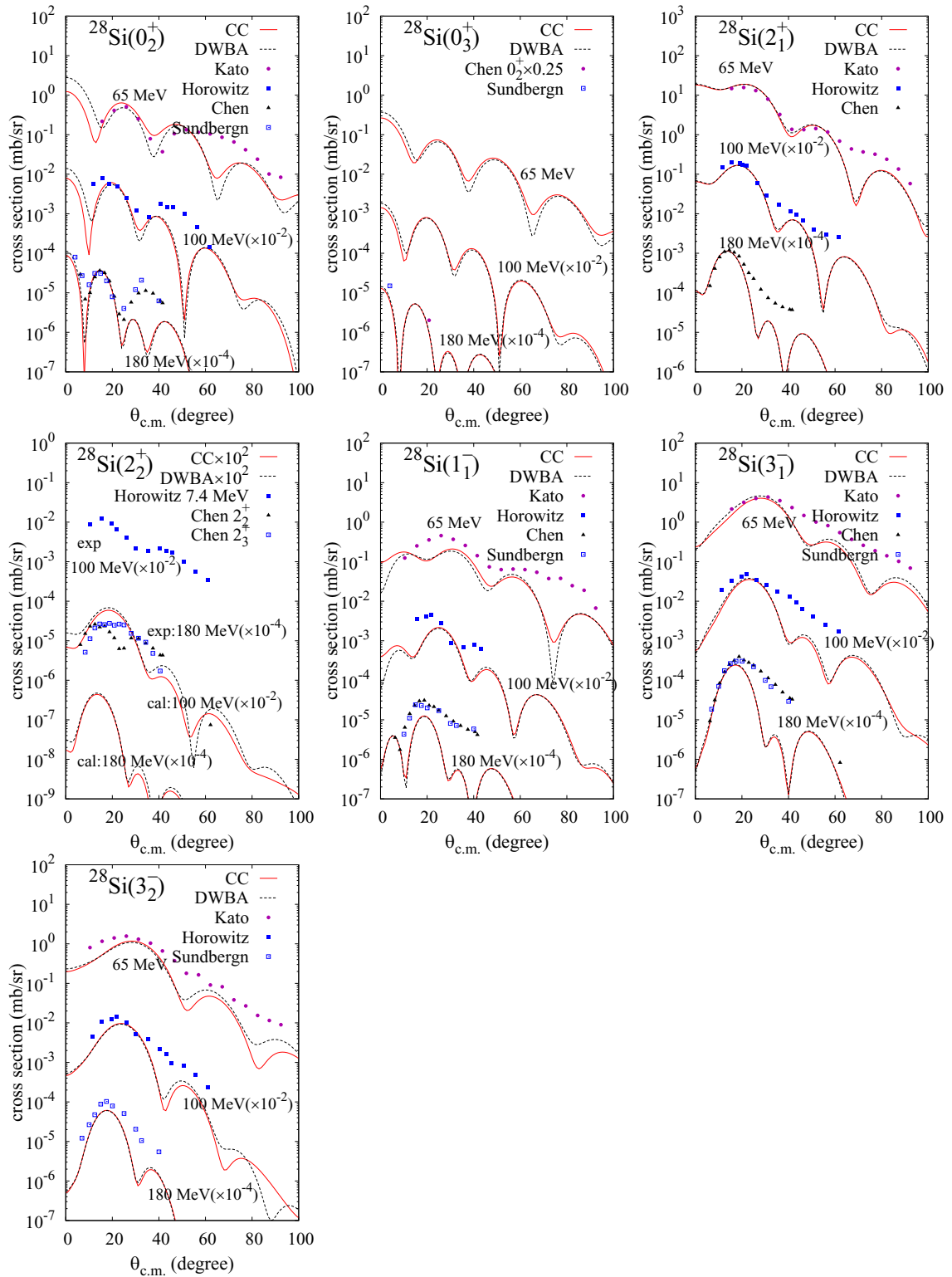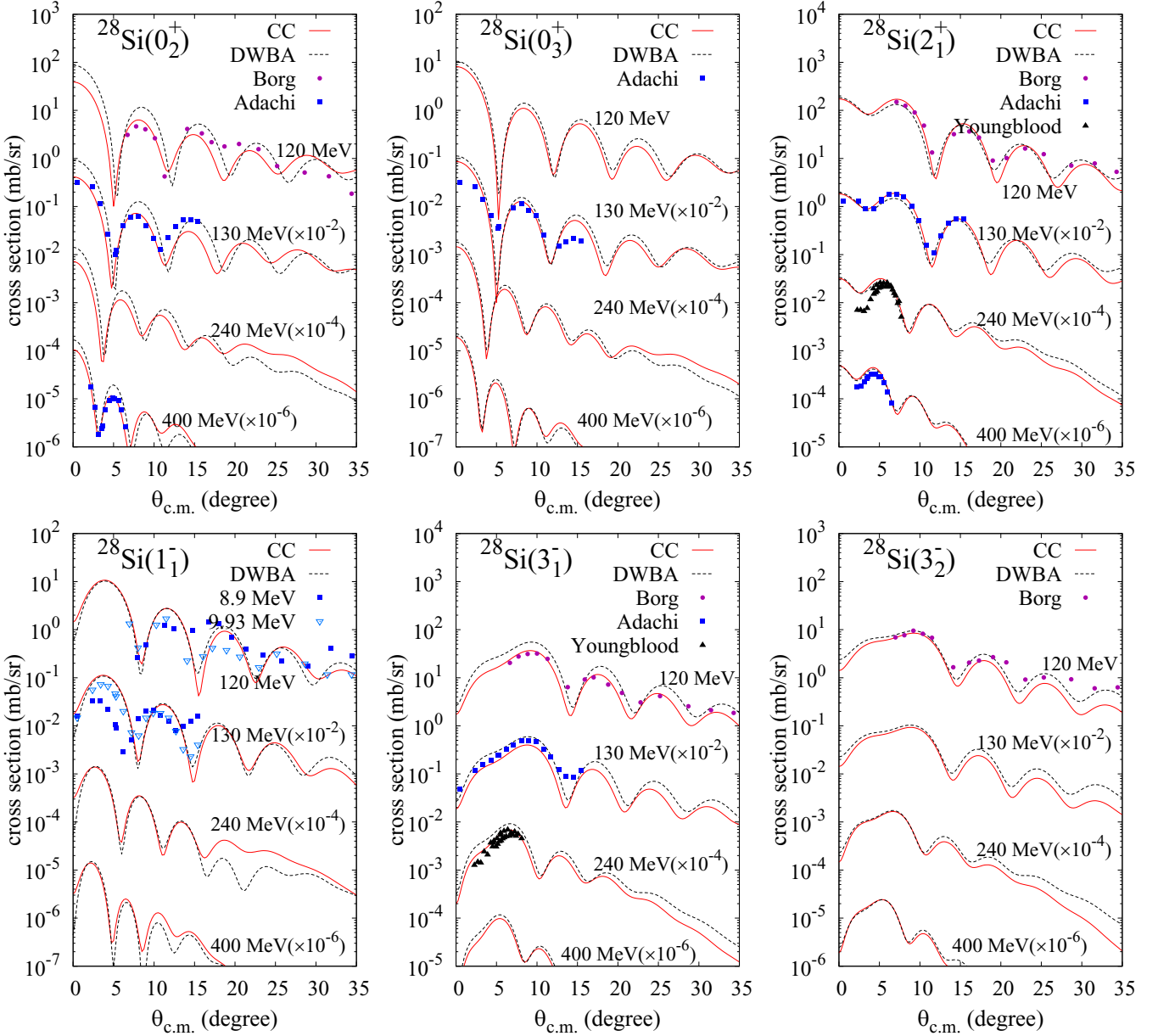
FIG. 8. Proton inelastic-scattering cross sections at incident energies $E_p = 65$, 100, 180 MeV obtained by the CC and DWBA calculations. Experimental data are cross sections at $E_p = 65$ MeV [13], $E_p = 100$ MeV [12], $E_p = 180$ MeV [14], and $E_p = 185$ MeV [11]. For the experimental data of the 0_3^+ cross sections, the upper limit of the 0_3^+ cross section at $\theta_{c.m.} = 4°$ from Ref. [11] and a quarter of the 0_2^+ cross section. at $\theta_{c.m.} = 20°$ evaluated from the observed spectrum shown in Ref. [14] are shown. See text.

FIG. 9. α inelastic-scattering cross sections at incident energies $E_\alpha = 120$, 130, 240, and 400 MeV obtained by the CC and DWBA calculations. Experiment data are (α, α') cross sections at $E_\alpha = 120$ MeV [59], 130 MeV [32], 240 MeV [19], and 386 MeV [32].

adopted transition densities. For 1^- states, the calculated 1_1^- cross sections reasonably agree with the experimental cross sections of the 1_1^- (8.9 MeV) state and also coincides with those of the 1_2^- (9.93 MeV) state. However, the experimental data are available only for low incident energies and not enough to draw a definite conclusion for assignment of the theoretical 1^- state.

V. DISCUSSION

In the previous sections, we showed the calculated results of form factors, p scattering, and α scattering and compared them with the observed data. In this section, we discuss transition properties of excited states by combining these

results of inelastic scattering as well as structure features such as transition strengths.

For the 0_2^+, 2_1^+, and 3_1^- states, details of transition properties such as $E\lambda$ transition strengths and form factors are experimentally known. The present calculation reasonably reproduces the experimental values of $B(E\lambda)$. After fine tuning by the renormalization, the experimental form factors are described well by the calculation. The MCC calculation with renormalized transition densities reproduces successfully α inelastic scattering in a wide energy range and reasonably describes the observed data of proton inelastic scattering. It should be stressed that we can obtain consistent results for electric and hadron scattering within a microscopic framework and confirm the applicability of the present MCC approach. Combining the structure analysis, these states are

understood as the 0^+, 2^+, and 3^- excitations built on the oblate ground state.

For the 0_3^+ state, there is no experimental information from electric probes such as form factors. Using the calculated transition density, which gives the strength $B(E0; 0_1^+ \rightarrow 0_3^+) = 0.7\ e^2\,\mathrm{fm}^4$, the present MCC calculation reproduces the α inelastic cross sections of the 0_3^+ state. It gives a result being consistent with the experimental observations of proton inelastic scattering. It should be commented again that the predicted transition strength may contain model ambiguity from state mixing of the vibration and prolate 0^+ modes. However, radial behavior (r dependence) of the 0^+ transition density is rather stable against such the state mixing and, therefore, the ambiguity may exist only in the overall factor of the $0_1^+ \rightarrow 0_3^+$ transition density. From the successful result for reproduction of the α inelastic-scattering data, we can say that the predicted value $B(E0; 0_1^+ \rightarrow 0_3^+) = 0.7\ e^2\,\mathrm{fm}^4$ is likely to be reasonable.

For 1^- states, inelastic form factors have been experimentally observed for the 1_1^- (8.9 MeV) and 1_2^- (9.93 MeV) states, but low-q data are not enough to determine the IS1 transition strength with high precision. In the structure calculation of AMD, the 1_{IS1}^- is obtained and regarded as the IS1 mode induced by α-cluster excitation on the oblate ground state. Since the calculated form factors are consistent with the experimental data observed for the 1_1^- (8.9 MeV) and 1_2^- (9.93 MeV) states, a possible assignment of this IS1 mode is either of the experimental 1^- states. Another possibility is that the IS1 mode is fragmented into the two 1^- states. The MCC calculation qualitatively describes proton-scattering data of the 1_1^- (8.9 MeV) state but the agreement is not sufficiently accurate. As for α scattering, the calculated cross sections of the 1_{IS1}^- state are in reasonable agreement with the (α, α') data of the 1_1^- (8.9 MeV) state and also with the data of the 1_2^- (9.93 MeV) state. In the present analysis, we cannot conclude which assignment is more likely.

The 3_2^- state is obtained as a member of the $K^\pi = 0^-$ band built on the 1_{IS1}^- state in the present calculation. The calculated form factors can be adjusted to the observed data of the 3_2^- (10.18 MeV) with a renormalization factor. For proton and α inelastic scattering, the 3_2^- cross sections obtained by the MCC calculation correspond well to the experimental cross sections observed for the 3_2^- (10.18 MeV) state. From this correspondence, the 3_2^- (10.18 MeV) is considered to be a member of the $K^\pi = 0^-$ band constructed on the IS1 mode, which is generated by the α-cluster excitation of the ground state.

The present calculation describes the shape coexistence of the oblate and prolate deformations. The prolate deformation constructs the rotational band of the 0_{pro}^+, 2_{pro}^+, and 4_{pro}^+ states. In the experimental energy spectra, there are two candidates for the prolate 2^+ state as the 2_2^+ (7.32 MeV) and 2_3^+ (7.42 MeV) states. The calculated $B(E2; 4_{\mathrm{pro}}^+ \rightarrow 2_{\mathrm{pro}}^+)$ of the in-band transition agrees well with a sum of the observed strengths $B(E2; 4_3^+ \rightarrow 2_2^+)$ and $B(E2; 4_3^+ \rightarrow 2_3^+)$, suggesting that the prolate 2^+ state is likely to be fragmented into two 2^+ states via mixing with other 2^+ components. In the present calculation for the 2_{pro}^+ state, inelastic transitions from the ground state are strongly suppressed because of the shape difference

between the initial and final states. As a result, weak form factors and inelastic scattering are obtained for the 2_{pro}^+ state. However, the observed form factors and proton-scattering cross sections of the 2_2^+ state are considerably large as two orders of magnitudes as the calculation. In other words, the significant form factors and proton inelastic cross sections can be understood as experimental signals of mixing of the other 2^+ component, which is beyond the present structure model calculation.

VI. SUMMARY

Transition properties of 0^+, 1^-, 2^+, and 3^- states of ^{28}Si were investigated via proton and α inelastic scattering. The structure calculation was performed with the energy variation after total angular-momentum and parity projections in the AMD framework. In the AMD calculation, the oblate ground and prolate bands, 0^+ and 3^- excitations, and the 1^- and 3^- states of the $K^\pi = 0^-$ band were obtained. The calculation reasonably reproduced the transition properties such as transition strengths and form factors.

Using the matter and transition densities of ^{28}Si obtained by the AMD calculation, the MCC calculations of proton and α scattering off ^{28}Si are performed. The proton-^{28}Si and α-^{28}Si potentials are microscopically derived by folding the Melbourne g-matrix NN interaction with the ^{28}Si and α densities. To reduce possible ambiguity from the structure model, the theoretical transition densities were renormalized to fit the $B(E\lambda)$ for the use of the MCC calculation. The MCC calculation reasonably reproduces the observed elastic and inelastic cross sections of proton and α scattering. From the analysis of inelastic scattering combined with structure properties, we assigned the theoretical states to the observed levels.

The 2_1^+, 0_2^+, and 3_1^- states are understood respectively as the oblate ground band member, vibration 0^+ and 3^- excitations built on the oblate ground state. The MCC calculation reproduces well the proton and α inelastic cross sections of these states in a wide energy range of $E_p = 65$–180 MeV and $E_\alpha = 120$–400 MeV. It should be stressed that consistent results for electron, proton, and α scatterings are obtained within a microscopic framework. These results prove the applicability of the present MCC approach for proton and α inelastic processes.

For the 0_3^+ state in the prolate band, the calculated $E0$ transition strength is relatively weak compared with that of the 0_2^+ state because of the shape difference between the oblate ground (initial) and prolate (final) states. The predicted strength, $B(E0; 0_1^+ \rightarrow 0_3^+) = 0.7\ e^2\,\mathrm{fm}^4$, is supported by the observed cross sections of α scattering. It is also consistent with the proton scattering.

In the structure calculation, the $K^\pi = 0^-$ band of the 1^- and 3^- states is constructed from the IS1 mode, which is induced by the α-cluster excitation of the oblate ground state. From the analysis of form factors and inelastic scattering, the 3^- state corresponds to the 3_2^- (10.18 MeV) state in the experimental spectra. The 1^- state is likely to be assigned to either of the 1_1^- (8.9 MeV) or 1_2^- (9.93 MeV) states, but we cannot draw a conclusion in the present analysis.

An advantage of the present MCC approach is that we can discuss electron, proton, and α inelastic scattering within a unified treatment of microscopic descriptions. Another merit is that there is no adjustable parameter in the reaction part. For given densities of a target nucleus, we can obtain the (p, p') and (α, α') cross sections at given energies without parameter tuning. Owing to such the straightforward connection between structure inputs and output cross sections, validity of a structure input can be examined via proton and α cross sections, even if electric data are not accurate enough. It has been proved that analysis of proton and α inelastic scattering with the MCC calculation using the microscopic structure calculation is a useful tool to investigate properties of excited states.

[1] S. Das Gupta and M. Harvey, Nucl. Phys. A **94**, 602 (1967).
[2] W. Bauhoff, H. Schultheis, and R. Schultheis, Phys. Rev. C **26**, 1725 (1982).
[3] H. Sagawa, X. R. Zhou, and X. Z. Zhang, Phys. Rev. C **72**, 054311 (2005).
[4] M. T. Win and K. Hagino, Phys. Rev. C **78**, 054311 (2008).
[5] B. N. Lu, E. G. Zhao, and S. G. Zhou, Phys. Rev. C **84**, 014328 (2011).
[6] Y. Kanada-En'yo, Phys. Rev. C **71**, 014303 (2005).
[7] Y. Taniguchi, Y. Kanada-En'yo, and M. Kimura, Phys. Rev. C **80**, 044316 (2009).
[8] Y. Chiba, Y. Taniguchi, and M. Kimura, Phys. Rev. C **95**, 044328 (2017).
[9] S. Yen, R. J. Sobie, T. E. Drake, H. Zarek, C. F. Williamson, S. Kowalski, and C. P. Sargent, Phys. Rev. C **27**, 1939 (1983).
[10] A. Nakada and Y. Torizuka, J. Phys. Soc. Jpn. **32**, 1 (1972).
[11] O. Sundberg, A. Johansson, G. Tibell, S. Dahlgren, D. Hasselgren, B. Höistad, A. Ingemarsson, and P.-U. Renberg, Nucl. Phys. A **101**, 481 (1967).
[12] Y. S. Horowitz, N. K. Sherman, and R. E. Bell, Nucl. Phys. A **134**, 577 (1969).
[13] S. Kato *et al.*, Phys. Rev. C **31**, 1616 (1985).
[14] Q. Chen, J. J. Kelly, P. P. Singh, M. C. Radhakrishna, W. P. Jones, and H. Nann, Phys. Rev. C **41**, 2514 (1990).
[15] M. N. Harakeh and A. van der Woude, *Giant Resonances* (Oxford University Press, London, 2001).
[16] D. H. Youngblood, P. Bogucki, J. D. Bronson, U. Garg, Y. W. Lui, and C. M. Rozsa, Phys. Rev. C **23**, 1997 (1981).
[17] H. L. Clark, Y.-W. Lui, D. H. Youngblood, K. Bachtr, U. Garg, M. N. Harakeh, and N. Kalantar-Nayestanaki, Nucl. Phys. A **649**, 57 (1999).
[18] D. H. Youngblood, Y.-W. Lui, and H. L. Clark, Phys. Rev. C **63**, 067301 (2001); **64**, 049901(E) (2001).
[19] D. H. Youngblood, Y.-W. Lui, and H. L. Clark, Phys. Rev. C **65**, 034302 (2002).
[20] B. John, Y. Tokimoto, Y.-W. Lui, H. L. Clark, X. Chen, and D. H. Youngblood, Phys. Rev. C **68**, 014305 (2003).
[21] D. H. Youngblood, Y.-W. Lui, H. L. Clark, Y. Tokimoto, and B. John, Phys. Rev. C **68**, 057303 (2003).
[22] M. Itoh *et al.*, Phys. Rev. C **68**, 064602 (2003).
[23] M. Uchida, H. Sakaguchi, M. Itoh, M. Yosoi, T. Kawabata, Y. Yasuda, H. Takeda, T. Murakami, S. Terashima, S. Kishi, U. Garg, P. Boutachkov, M. Hedden, B. Kharraja, M. Koss, B. K. Nayak, S. Zhu, M. Fujiwara, H. Fujimura, H. P. Yoshida *et al.*, Phys. Rev. C **69**, 051301(R) (2004).

[24] Y.-W. Lui, D. H. Youngblood, H. L. Clark, Y. Tokimoto, and B. John, Phys. Rev. C **73**, 014314 (2006).
[25] D. H. Youngblood, Y.-W. Lui, and H. L. Clark, Phys. Rev. C **76**, 027304 (2007).
[26] T. Li *et al.*, Phys. Rev. Lett. **99**, 162503 (2007).
[27] M. Itoh *et al.*, Phys. Rev. C **88**, 064313 (2013).
[28] D. H. Youngblood, Y.-W. Lui, Krishichayan, J. Button, G. Bonasera, and S. Shlomo, Phys. Rev. C **92**, 014318 (2015).
[29] T. Peach *et al.*, Phys. Rev. C **93**, 064325 (2016).
[30] J. Button, Y. W. Lui, D. H. Youngblood, X. Chen, G. Bonasera, and S. Shlomo, Phys. Rev. C **96**, 054330 (2017).
[31] Y. K. Gupta *et al.*, Phys. Rev. C **97**, 064323 (2018).
[32] S. Adachi *et al.*, Phys. Rev. C **97**, 014601 (2018).
[33] Y. Suzuki and S. Hara, Phys. Rev. C **39**, 658 (1989).
[34] T. Kawabata, H. Akimune, H. Fujita, Y. Fujita, M. Fujiwara, K. Hara, K. Hatanaka, M. Itoh *et al.*, Phys. Lett. B **646**, 6 (2007).
[35] T. Wakasa *et al.*, Phys. Lett. B **653**, 173 (2007).
[36] M. Itoh *et al.*, Phys. Rev. C **84**, 054308 (2011).
[37] T. Yamada, Y. Funaki, T. Myo, H. Horiuchi, K. Ikeda, G. Ropke, P. Schuck, and A. Tohsaki, Phys. Rev. C **85**, 034315 (2012).
[38] Y. Chiba, M. Kimura, and Y. Taniguchi, Phys. Rev. C **93**, 034319 (2016).
[39] Y. Kanada-En'yo and K. Ogata, Phys. Rev. C **99**, 064601 (2019).
[40] Y. Kanada-En'yo and K. Ogata, Phys. Rev. C **99**, 064608 (2019).
[41] Y. Kanada-En'yo, H. Horiuchi, and A. Ono, Phys. Rev. C **52**, 628 (1995).
[42] Y. Kanada-En'yo, Phys. Rev. Lett. **81**, 5291 (1998).
[43] Y. Kanada-En'yo, M. Kimura, and A. Ono, Prog. Theor. Exp. Phys. **2012**, 01A202 (2012).
[44] Y. Kanada-En'yo and K. Ogata, Phys. Rev. C **100**, 064616 (2019).
[45] K. Amos, P. J. Dortmans, H. V. von Geramb, S. Karataglidis, and J. Raynal, Adv. Nucl. Phys. **25**, 275 (2000).
[46] K. Minomo, K. Ogata, M. Kohno, Y. R. Shimizu, and M. Yahiro, J. Phys. G **37**, 085011 (2010).
[47] M. Toyokawa, K. Minomo, and M. Yahiro, Phys. Rev. C **88**, 054602 (2013).
[48] K. Minomo, K. Washiyama, and K. Ogata, arXiv:1712.10121.
[49] K. Egashira, K. Minomo, M. Toyokawa, T. Matsumoto, and M. Yahiro, Phys. Rev. C **89**, 064611 (2014).
[50] K. Minomo and K. Ogata, Phys. Rev. C **93**, 051601(R) (2016).
[51] T. Ando, K. Ikeda, and A. Tohsaki, Prog. Theor. Phys. **64**, 1608 (1980).

[52] R. Tamagaki, Prog. Theor. Phys. **39**, 91 (1968).

[53] N. Yamaguchi, T. Kasahara, S. Nagata, and Y. Akaishi, Prog. Theor. Phys. **62**, 1018 (1979).

[54] R. Machleidt, K. Holinde, and Ch. Elster, Phys. Rep. **149**, 1 (1987).

[55] G. R. Satchler and W. G. Love, Phys. Rep. **55**, 183 (1979).

[56] M. Shamsuzzoha Basunia, Nucl. Data Sheets **114**, 1189 (2013).

[57] I. Angeli and K. P. Marinova, At. Data Nucl. Data Tables **99**, 69 (2013).

[58] P. Schwandt, H. O. Meyer, W. W. Jacobs, A. D. Bacher, S. E. Vigdor, M. D. Kaitchuck, and T. R. Donoghue, Phys. Rev. C **26**, 55 (1982).

[59] K. Van Der Borg, M. N. Harakeh, and A. Van Der Woude, Nucl. Phys. A **365**, 243 (1981).

[60] Y. K. Kwon, C. S. Lee, and S. Kubono, J. Korean Phys. Soc. **51**, 1635 (2007).